

# ANALYSIS OF DIFFERENT PROCESS NOISE MODELS IN TYPICAL ORBIT DETERMINATION SCENARIOS

M. Schubert<sup>(1)</sup>, C. Keschull<sup>(2)</sup>, and S. Horstmann<sup>(1)</sup>

<sup>1</sup>*Institute of Space Systems, 38108 Braunschweig, Germany, Email: {manuel.schubert, s.horstmann}@tu-braunschweig.de*

<sup>2</sup>*OKAPI:Orbits, 38106 Braunschweig, Germany, Email: christopher.kebschull@okapiorbits.com*

## ABSTRACT

Orbit determination is a crucial part of Space Situational Awareness, especially, in the wake of upcoming mega constellations and the general trend towards an increased rate of orbital injections. While there are several initial and statistical orbit determination algorithms, one key aspect is the precise modeling of the process noise to accurately capture the error between the used equations to describe the orbit mechanics and reality. Two widely used methods to model the process noise are state noise compensation (SNC) and dynamic model compensation (DMC). More recently, adaptive methods, such as the covariance matching (CM) or adaptive state noise compensation (ASNC), have been developed [1].

In this paper, an analysis of statistical orbit determination using SNC, CM, and ASNC is shown. Hereby, the Radar System Simulator (RSS) that was developed at the Institute of Space Systems at the TU Braunschweig was used to simulate typical scenarios. Therefore, tracklets of an exemplary space debris object population were simulated. Using these tracklets, the above mentioned process noise methods were applied in combination with multiple statistical orbit determination methods, such as the Unscented Kalman Filter (UKF) or Cubature Kalman Filter (CKF).

Primarily, the performed simulations have shown that the process noise indeed is a critical aspect influencing the accuracy of any orbit determination. In order to achieve realistic results, i.e. convergence between estimated and real state as well as a consistent covariance, realistically reflecting the quality of the estimate, the process noise needs to be tuned adequately for the respective situation. Applying a tuning process of the SNC can significantly improve the quality of the orbit determination and achieve results that are closer to reality. Unfortunately, the SNC needs to be tuned offline with a priori knowledge of the adequate parameters. These correct tuning parameters, however, are usually not known beforehand for any given scenario. Therefore, adaptive methods could be the key to perform accurate orbit determinations regardless of the actual scenario.

This paper will show the results of process noise variants in combination with different orbit determination algorithms with regard to the convergence of estimated and real state as well as covariance truth. It will conclude with a comparison of the three stated approaches.

Keywords: TU Braunschweig; OKAPI:Orbits; Orbit Determination; Process Noise; SNC; ASNC; CM.

## 1. INTRODUCTION

With regard to the continuously increasing number of controlled and uncontrolled, i.e. space debris, objects in Earth's orbit, orbit determination is one of the key components of a Space Situational Awareness (SSA) process chain and, thus, tracking the developments in the space environment. Hence, it is constantly worthwhile to improve the existing algorithms, such as the Extended Kalman Filter (EKF), the UKF or the CKF. One aspect affecting the performance of these precise orbit determination (POD) algorithms is the process noise. Traditional models of the process noise are SNC or DMC, while more recently CM or ASNC have been developed. While the former have to be tuned offline according to the actual situation, the latter adjust themselves adaptively. Potentially, such adaptive methods could improve the performance of orbit determination algorithms significantly. In order to test these more recent developments in typical orbit determination applications, adaptive process noise models have been implemented within the RSS, a simulator environment that was developed at the Institute of Space Systems at the TU Braunschweig and is capable of producing realistic observations and tracklets of space debris objects (SDOs). Further, it allows the application of different initial orbit determination (IOD) and POD algorithms which includes modeling the process noise. Using the traditional and more recent process noise models, a variety of simulations have been performed to test their performance.

In the following, there will be a short summary of the underlying theoretical background and a description of the

carried out simulations. Further, the results of these simulations will be shown and a conclusion is drawn at the end.

## 2. BACKGROUND

Within the POD algorithms based on Kalman filtering generally two main sources for noise have to be taken into account, the measurement noise and the process noise. While the measurement noise is directly connected to the measurement process and the corresponding sensor systems, the process noise stems from modeling the real world which inherently leads to uncertainties and noise. This is due to complex orbit perturbations affecting the space object dynamics and the corresponding accelerations that can not be modeled perfectly. To account for the unknown accelerations, the process noise methods propagate a noise matrix alongside the propagated state covariance. Afterwards both matrices are combined and yield a larger covariance in comparison to the state covariance alone in order to account for the unknown errors [2]. Often the measurement noise is known by the operators of sensor systems such as radars or telescopes and can therefore be taken into account accordingly. In contrast, the process noise is usually not known and most of the traditional models have to be tuned offline according to the combination of SDOs and its properties, its orbit and the used POD. A desirable solution to this could be adaptive models that tune the process noise parameters online as needed to represent the real, unknown magnitude of noise.

### 2.1. Process Noise

The process noise models that are used in Kalman filtering, to compensate for the complex spacecraft dynamics that cannot be modeled perfectly, can roughly be divided into non-adaptive and adaptive methods. Further, SNC and DMC are distinguished (see [3]).

The base of POD algorithms, such as the UKF or CKF, is an estimation of the state for a nonlinear dynamical system [4]:

$$x_{k+1} = f(k, x_k) + w_k, \quad (1)$$

$$y_k = h(k, x_k) + v_k, \quad (2)$$

where  $x_k$  and  $y_k$  represent the state and measurement at point  $k$  respectively while  $w_k$  and  $v_k$  are the process and measurement noise respectively. For a complete description of the UKF and CKF see, for instance, [4] and [5] respectively. In the context of this work, the relevant part is the process noise  $w_k$ . The term SNC describes the assumption that  $w(t)$  is white noise with a constant covariance that is known [3]. This means that the state dynamics are assumed to be influenced by a stochastic acceleration with mean zero and constant standard deviation. The resulting process noise covariance matrix, as

also used in the RSS, is described as [3]:

$$Q(t) = \sigma^2 \cdot \begin{bmatrix} \frac{1}{3} (t - t_0)^3 & \frac{1}{2} (t - t_0)^2 \\ \frac{1}{2} (t - t_0)^2 & (t - t_0) \end{bmatrix}, \quad (3)$$

where the standard deviation  $\sigma$  is predefined by the user and has to be tuned accordingly. For DMC an acceleration described by a first-order linear stochastic differential equation is assumed [3].

Another approach that can be used to model the process noise is CM, covariance matching. As an adaptive method, CM has the advantage to avoid the necessity of a priori knowledge as is needed, for instance, in the SNC method [6, 7]. This CM technique estimates the process noise covariance from historical values of the state prediction and state estimation and the corresponding state innovation and residuals. Hereby, the considered values can either encompass all historical values or all values inside a specified window [7]. The specific formulation of the CM technique exists in multiple versions [1, 7]. Within the RSS it is implemented under the assumption of a steady state which leads to an estimated process noise covariance of [1]:

$$Q_k = \frac{1}{N} \sum_{j=k-N}^{k-1} \tilde{y}_j \tilde{y}_j^T, \quad (4)$$

where  $N$  is the window length and  $\tilde{y}$  is the state innovation, the difference between the real and predicted values [7]. A state innovation scaling factor can be set as an additional tuning parameter.

Both previously explained methods, SNC and CM, can be combined into an adaptive state noise compensation, the ASNC [1]. The same can be done for DMC and CM to obtain an adaptive dynamic model compensation, ADMC. Analog to CM the ASNC approach starts by calculating an estimated process noise covariance  $\hat{Q}_k$  via Equation 4. For the next step a theoretical state innovation covariance  $\Sigma_K$  has to be calculated from the Kalman Gain  $K_k$  and the measurement innovation covariance  $P_{yy,k}$  [1]:

$$\Sigma_K = K_k \cdot P_{yy,k} \cdot K_k^T \quad (5)$$

It is needed to calculate a weighting matrix for the single components of the final process noise covariance matrix which is obtained, in accordance to Equation 3, by [1]:

$$Q_k = \begin{bmatrix} \frac{1}{3} \Delta t^3 \tilde{Q}_k & \frac{1}{2} \Delta t^2 \tilde{Q}_k \\ \frac{1}{2} \Delta t^2 \tilde{Q}_k & \Delta t \tilde{Q}_k \end{bmatrix} \quad (6)$$

Hereby, the estimated matrix  $\tilde{Q}_k$  is obtained by solving [1]

$$\tilde{Q}_{k,i,i} = \max \left( 0, \frac{\bar{X}(i)^T \bar{W}(i)^{-1} b(i)}{\bar{X}(i)^T \bar{W}(i)^{-1} \bar{X}(i)} \right) \quad (7)$$

element-wise for the diagonal entries of  $\tilde{Q}_k$ , where [1]

$$\bar{X}(i) = \begin{pmatrix} \frac{1}{3} \Delta t^3 \\ \frac{1}{2} \Delta t^2 \\ \Delta t \end{pmatrix}, \quad b(i) = \begin{pmatrix} \hat{Q}_{k,i,i} \\ \hat{Q}_{k,i+3,i} \\ \hat{Q}_{k,i+3,i+3} \end{pmatrix} \quad (8)$$

and the diagonal matrix [1]

$$\bar{W}(i) = \sum_{p=k-N+1}^k \begin{bmatrix} \bar{\Sigma}_{p,i,i} & 0 & 0 \\ 0 & \bar{\Sigma}_{p,i+3,i} & 0 \\ 0 & 0 & \bar{\Sigma}_{p,i+3,i+3} \end{bmatrix}, \quad (9)$$

where  $N$  is again the window length as introduced in the CM method.

## 2.2. Assessment of the covariance truth

While evaluating the results of the PODs, additionally to absolute errors, such as deviations in radial, along-track and cross-track directions, the consistency of the filter and the resulting covariances is an important criterion as well. Hereby, two general considerations apply. On the one hand, the estimate errors should be acceptable mean and the calculated covariance should match these errors. On the other hand, the innovations of the filter should have the same property and should be acceptable white. The consistency of the filter can be evaluated using statistical tests. One option is the time-averaged Normalized Estimation Error Squared (NEES), which is defined as the following summation over all states  $k$  [8]:

$$\bar{\varepsilon}_x = \frac{1}{K} \sum_{k=1}^K (x_k - \hat{x}_k)' P_k^{-1} (x_k - \hat{x}_k). \quad (10)$$

Hereby,  $\hat{x}_k$  is the estimated state of the filter with respect to the true state  $x_k$ .  $P_k$  is the covariance of the estimated state.  $K \cdot \bar{\varepsilon}_x$  has a  $\chi^2$ -distribution with a degree of freedom of  $K \cdot n_x$ , where  $n_x$  is the dimension of the state which is 6 for the 3 position and 3 velocity components as relevant for the implementation in the RSS. Another option is using the time-averaged Normalized Innovation Squared (NIS) [8]:

$$\bar{\varepsilon}_y = \frac{1}{K} \sum_{k=1}^K (y_k - \hat{y}_k)' P_{yy,k}^{-1} (y_k - \hat{y}_k), \quad (11)$$

where  $y_k$  is the measured state. Further,  $\hat{y}_k$  is the propagated and into the measurement space transformed state, while the innovation covariance is  $P_{yy,k}$ . In this case,  $K \cdot \bar{\varepsilon}_y$  has a  $\chi^2$ -distribution with  $K \cdot n_y$  degrees of freedom, where  $n_y$  is the dimension of the measurement. In this paper and the context of the RSS, the measurement consists of 4 dimensions: Azimuth, Elevation, Range and Range Rate. Both values resulting from the Equations 10 and 11 represent a summation of the squared Mahalanobis distances for each state  $k$  [2].

Based on these parameters, a  $\chi^2$ -test can be done. The parameters  $K \cdot \bar{\varepsilon}_x$  or  $K \cdot \bar{\varepsilon}_y$  have to be in a certain acceptance interval around the expected value. The expected value equals the degree of freedom of the  $\chi^2$ -distribution and equals 6 for the NEES,  $\bar{\varepsilon}_x$ , and 4 for the NIS,  $\bar{\varepsilon}_y$ , respectively. In this case the filter is consistent. If the parameter is larger than the upper bound, the calculated

error might be too large or the covariance too small. In this case the filter might be too optimistic. And by analogy if the lower bound is exceeded the filter might be too pessimistic [8]. The distances between the expected value and the lower and upper bounds of the acceptance interval depend on the number of states  $k$  and the percentile specified for the acceptance interval.

## 3. SIMULATIONS

In order to test and evaluate the previously described methods to model the process noise, several simulations have been performed within the RSS environment in combination with the UKF and CKF. Hereby, errors in position and velocity, the covariance matrices, and the statistical tests for the covariance truth, NEES and NIS, were taken into account for the evaluation. To provide constant conditions for the simulations as far as possible, the same objects were used to generate observations and tracklets for the orbit determination throughout all simulations. These objects were taken from the Meteoroid and Space Debris Terrestrial Environment Reference (MASTER) object population and listed in Tables 1 and 2.

Table 1. Physical properties of the objects used as basis for the generation of observations and orbit determination.

ID	Mass	Diameter	Mass to area ratio
[-]	[kg]	[m]	[kg m <sup>-2</sup> ]
1	823.6	2.125	232.193
2	2615	4.098	198.286
3	800	6.368	25.122
4	65.41	2.257	16.352
5	4006	5.643	160.170

Table 2. Orbit properties of the objects used as basis for the generation of observations and orbit determination.  $a$ : semi-major axis,  $\varepsilon$ : eccentricity,  $i$ : inclination,  $\Omega$ : right ascension of the ascending node,  $\omega$ : argument of the perigee.

ID	$a$	$\varepsilon$	$i$	$\Omega$	$\omega$
[-]	[km]	[-]	[°]	[°]	[°]
1	7140.8	0.0072	98.60	258.88	4.31
2	7141.2	0.0001	98.53	18.50	185.06
3	7147.8	0.0036	98.35	314.06	271.72
4	7140.0	0.0036	98.67	126.12	263.45
5	7148.9	0.0019	98.48	314.18	262.37

All of these objects are, as can be seen from the orbit parameters, in a Sun-synchronous orbit (SSO). While including a range of mass to area ratios, big objects were chosen, to guarantee high probabilities of good observations. In order to obtain observations the Tracking

and Imaging Radar (TIRA) that is located in Wachtberg was simulated within the radar performance model of the RSS. Hereby, the TIRA system was located at a longitude of  $16.03^\circ$ , a latitude of  $78.15^\circ$  and an altitude of 445 m. This corresponds to a radar site of the European Incoherent Scatter Scientific Association (EISCAT) at Longyearbyen. It was chosen to further optimize the conditions for good observations of objects in an SSO. For all performed simulations an observation campaign was carried out over seven days, leading to approximately 100 000 detections and 500 reliable tracklets.

Regarding the SNC mainly two iterations of simulations have been performed varying the tuning parameter  $\sigma$  (see Equation 3). Based on previous analyses, the standard deviation  $\sigma$  was varied between  $1 \times 10^{-6} \text{m s}^{-3/2}$  and  $2 \times 10^{-2} \text{m s}^{-3/2}$ . In both iterations this was done in three equidistant steps,  $9 \times 10^{-3}$ ,  $1.45 \times 10^{-2}$ , and  $2 \times 10^{-2} \text{m s}^{-3/2}$  for the first iteration and  $1 \times 10^{-6}$ ,  $1 \times 10^{-5}$ , and  $1 \times 10^{-4} \text{m s}^{-3/2}$  for the second iteration. Hereby, the standard deviation was tuned separately for each component of the state vector, three position and three velocity components, leading to a total of 729 ( $3^6$ ) combinations for each of the two iterations.

For the CM and ASNC methods, three tuning parameters have been taken into account:

1. Window length
2. State innovation scaling factor (SISF)
3. Propagated covariance scaling factor (PCSF)

Hereby, the window length was varied between 5 and 100 steps, i.e. the number of previous observations taken into account, in combination with different state innovation and propagated covariance scaling factors (no variation between position and velocity components). Finally, in a more elaborate analysis the ASNC method was evaluated for component-wise variations of the state innovation scaling factor in the same manner as described before for the SNC standard deviation. In this case, again two iterations of simulations have been performed. First, all components have been varied between values of 0.5 and  $2/3$  ( $2^6 = 64$  combinations). Since, the influence of the velocity components was negligible in the first iteration, only the three position components were varied in the second iteration. This time in five steps: 0.1, 0.2, 0.3, 0.4, and 0.5 ( $5^3 = 125$  combinations). During these two iterations, the window length and propagated covariance scaling factor have been kept fixed at 5 and 1.5 respectively.

#### 4. RESULTS AND DISCUSSION

After describing the simulations, the results will be presented in the same order in the following, starting with the variations of the tuning parameters for the SNC. For a better comparability the majority of the results will be

shown for object number 2 which was randomly chosen. Since the results are qualitatively very close for all objects, the corresponding results for object 2 are representative for all simulations. To evaluate the results three plots will be shown for each simulation that is presented, including the root-mean-square error (RMSE) of the position, the NEES, and the NIS. This ensures a complete picture containing the overall accuracy and the covariance truth. The RMSE between the estimated ( $\hat{x}$ ) and actual state ( $x$ ) is calculated over all states  $k$ , where  $K$  is the total number of states:

$$RMSE = \sqrt{\frac{\sum_{k=1}^K (\hat{x}_k - x_k)^2}{K}}. \quad (12)$$

Regarding the SNC variations such a set of three plots is shown for both of the iterations. Hereby, the RMSE in the UVW coordinates is shown in the Figures 1 and 2 for iteration 1 and 2 respectively, the NEES is shown in the Figures 3 and 4 for iteration 1 and 2 respectively and the NIS is shown in the Figures 5 and 6 for iteration 1 and 2 respectively. All these plots show the results using the UKF and visualize the 729 combinations for each iteration within a heatmap while the x- and y- axis represent the corresponding combination of the six standard deviation components that are varied and the color depicts the error size. Since this type of visualization might not be intuitive from the start, it should be explained briefly. For both iterations three values were used to vary all six components of the standard deviation in all possible combinations. These three values are represented by a “1” for the lowest value, a “2” for the medium value and a “3” for the highest value. An exemplary sequence of the digits “221131” would represent a position components vector of  $(1.45 \times 10^{-2}, 1.45 \times 10^{-2}, 9 \times 10^{-3})^T$  and a velocity components vector of  $(9 \times 10^{-3}, 2 \times 10^{-2}, 9 \times 10^{-3})^T$  for the first iteration.

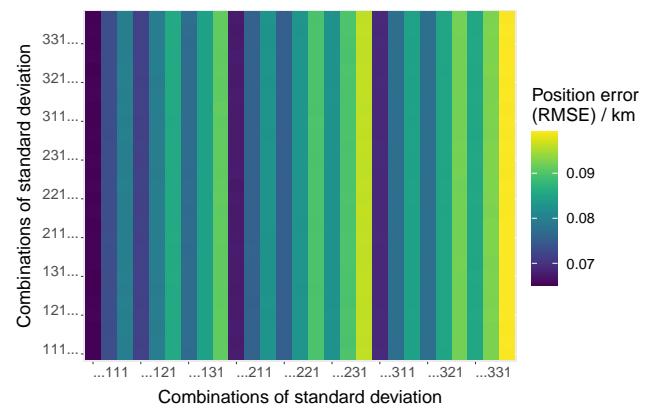


Figure 1. Position error in UVW (RMSE) of object 2 for different combinations of the standard deviation components that define the process noise for the SNC (UKF, 1. iteration). The x-axis shows the combinations of the velocity components, while the y-axis shows the combinations of the position components. This heatmap displays all 729 combinations. “1” =  $9 \times 10^{-3} \text{m s}^{-3/2}$ , “2” =  $1.45 \times 10^{-2} \text{m s}^{-3/2}$ , “3” =  $2 \times 10^{-2} \text{m s}^{-3/2}$ .

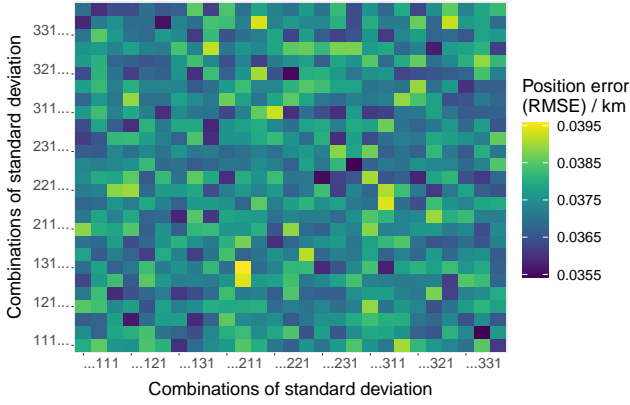


Figure 2. Position error in UVW (RMSE) of object 2 for different combinations of the standard deviation components that define the process noise for the SNC (UKF, 2. iteration). The x-axis shows the combinations of the velocity components, while the y-axis shows the combinations of the position components. This heatmap displays all 729 combinations. “1” =  $1 \times 10^{-6} \text{m s}^{-3/2}$ , “2” =  $1 \times 10^{-5} \text{m s}^{-3/2}$ , “3” =  $1 \times 10^{-4} \text{m s}^{-3/2}$ .

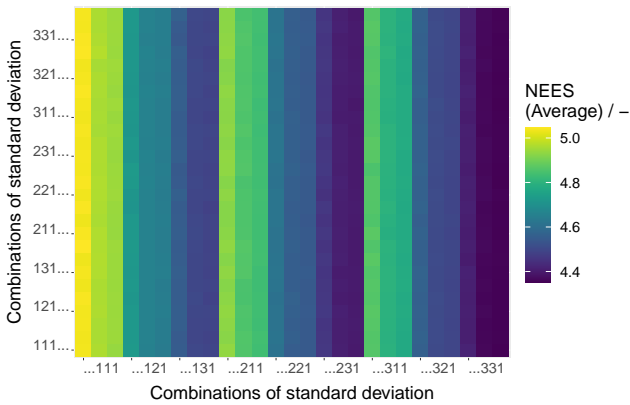


Figure 3. NEES of object 2 for different combinations of the standard deviation components that define the process noise for the SNC (UKF, 1. iteration). The x-axis shows the combinations of the velocity components, while the y-axis shows the combinations of the position components. This heatmap displays all 729 combinations. “1” =  $9 \times 10^{-3} \text{m s}^{-3/2}$ , “2” =  $1.45 \times 10^{-2} \text{m s}^{-3/2}$ , “3” =  $2 \times 10^{-2} \text{m s}^{-3/2}$ .

Comparing the first and second iteration all plots concerning the first iteration show a pattern representing a sensitivity of the results mostly with regard to the velocity components of the standard deviation (x-axis). Hereby, the lowest value for the y and z components yield the lowest errors and the lowest standard deviation value for all velocity components yields the best NEES (closest to the ideal of 6) value. In contrast, the best NIS results (closest to the ideal of 4) is obtained in iteration 1 by using the highest standard deviation values for the velocity components. However, the NIS value varies very little over all 729 combinations. This observed pattern is not seen

in the plots regarding iteration 2. Here, more equally distributed RMSE, NEES and NIS values are found. Hereby, the error is, generally, much lower in comparison with the first iteration while the NEES, with values around 50 to 60 diverges much further from the ideal value. While the same bigger discrepancy between ideal value and obtained values can be seen for the NIS in the second iteration, the differences between the iterations is only slight in this case.

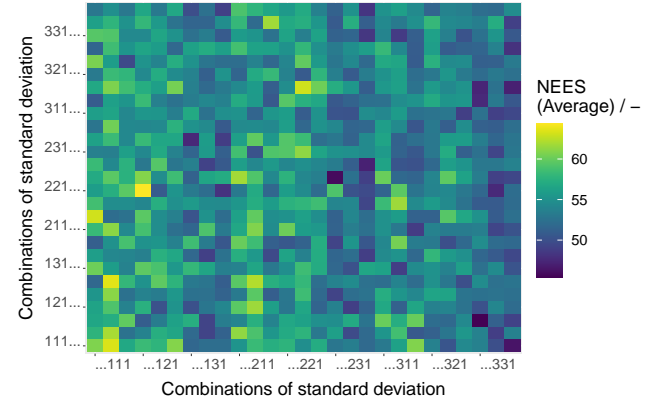


Figure 4. NEES of object 2 for different combinations of the standard deviation components that define the process noise for the SNC (UKF, 2. iteration). The x-axis shows the combinations of the velocity components, while the y-axis shows the combinations of the position components. This heatmap displays all 729 combinations. “1” =  $1 \times 10^{-6} \text{m s}^{-3/2}$ , “2” =  $1 \times 10^{-5} \text{m s}^{-3/2}$ , “3” =  $1 \times 10^{-4} \text{m s}^{-3/2}$ .

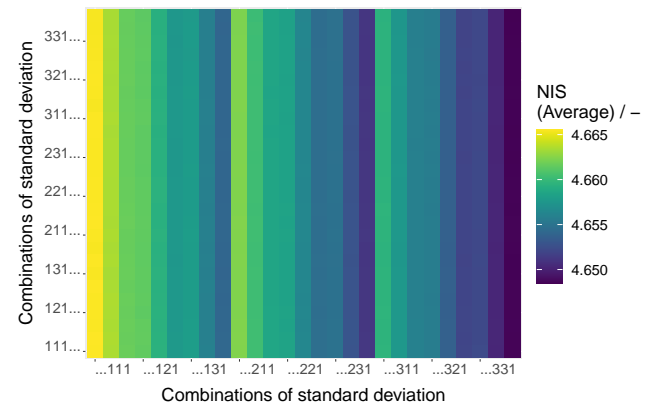


Figure 5. NIS of object 2 for different combinations of the standard deviation components that define the process noise for the SNC (UKF, 1. iteration). The x-axis shows the combinations of the velocity components, while the y-axis shows the combinations of the position components. This heatmap displays all 729 combinations. “1” =  $9 \times 10^{-3} \text{m s}^{-3/2}$ , “2” =  $1.45 \times 10^{-2} \text{m s}^{-3/2}$ , “3” =  $2 \times 10^{-2} \text{m s}^{-3/2}$ .

To summarize the results of the SNC simulations, lowering the values of the standard deviation components used

as tuning parameters within the first iteration yields better results regarding the RMSE of the position and the NEES, while the obtained NIS values worsen slightly. Lowering these values much further, as done in the second iteration yields much lower RMSEs for the position, but the filter consistency deteriorates, especially concerning the NEES. Such high values for the NEES suggest a too small covariance matrix and an accordingly too optimistic estimate of the filter. Further, the optimal NEES and NIS values tend to be obtained by opposing standard deviation values. This is especially true for iteration 1 and it indicates that a trade-off has to be made here.

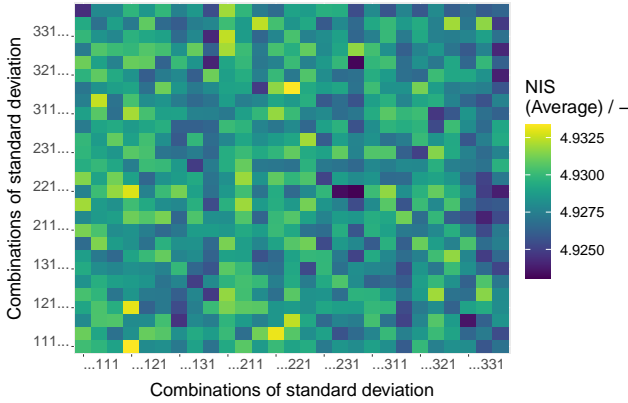


Figure 6. NIS of object 2 for different combinations of the standard deviation components that define the process noise for the SNC (UKF, 2. iteration). The x-axis shows the combinations of the velocity components, while the y-axis shows the combinations of the position components. This heatmap displays all 729 combinations. “1” =  $1 \times 10^{-6} \text{m s}^{-3/2}$ , “2” =  $1 \times 10^{-5} \text{m s}^{-3/2}$ , “3” =  $1 \times 10^{-4} \text{m s}^{-3/2}$ .

Regarding the CM method the analysis was, as mentioned in Section 3, performed with respect to the scaling factors PCSF and SISF as well as the window length. To represent the variation of the orbit determination methods as well, the results for the CM are shown both for the UKF and the CKF in this case. The following plots show the results for 4 different combinations of the PCSF and SISF while the corresponding simulations were performed for a varying window length between 5 and 100 (5 to 50 in one case) for the sliding window method of the CM. Once more the results are analyzed by evaluating both the absolute errors and the filter consistency parameters. Therefore, the RMSE of the position error is shown in the Figures 7 and 8 for the UKF and CKF respectively while the NEES values are shown in Figure 9 and 10 for the UKF and CKF respectively and the NIS values are shown in Figure 11 and 12 for the UKF and CKF respectively. Hereby, the x-axis shows the varying window length and the y-axis represents the RMSE, NEES or NIS.

In the case of the RMSE, the results of the UKF and CKF vary only very slightly. The lowest error can be achieved by a combination of PCSF = 1.5 and SISF = 2/3 (yellow data row). By setting the PCSF to 1 and increasing the

SISF, the error increases as well. Additionally, the error tends to increase, in general, with an increasing window size. This trend would also be expected for window sizes bigger than 50 in the case of the yellow data row. Simulations with higher window sizes were not performed in this case, since the window size was originally limited to 50 for this analysis, but later increased to 100 for the other parameter combinations.

As could already be seen in the results of the SNC analysis, the settings for the lowest error are not necessarily the settings for the best results with respect to achieving realistic results that are consistent with the covariances. Therefore, it is important to evaluate the NEES and NIS values for the same parameter combinations.

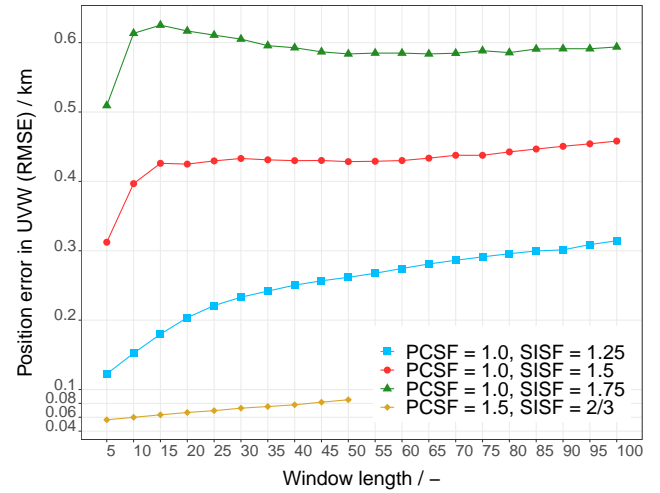


Figure 7. Position error in UVW (RMSE) of object 2 for different combinations of the SISF and PCSF that define the process noise for the CM (UKF).

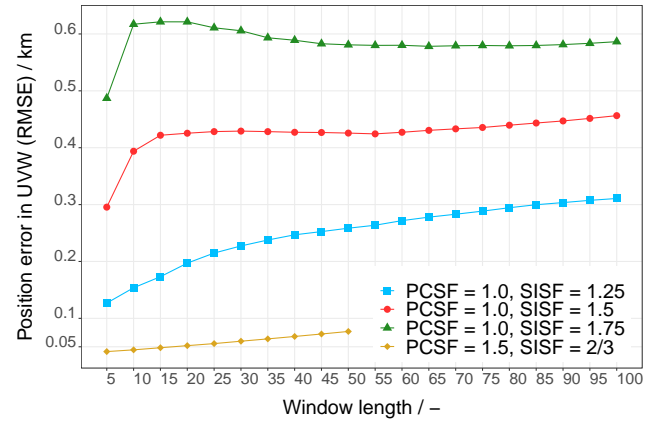


Figure 8. Position error in UVW (RMSE) of object 2 for different combinations of the SISF and PCSF that define the process noise for the CM (CKF).

Comparing the NEES values for the UKF and CKF simulations, the values differ more significantly as was the

case for the RMSE. While the overall trends are similar between the orbit determination methods, the best results are achieved for a combination of PCSF = 1.0 and SISF = 1.75 (green data row in Figure 9) for the UKF. In contrast, very good results with an NEES close to 6 can be achieved for almost all combinations of the scaling factors in the case of the CKF by adjusting the window size. For a window size of 5 the red and yellow data rows (Figure 10) show the best results, while the closest NEES to the ideal value of 6 for a window size of 10 is obtained by the blue data row (PCSF = 1.0, SISF = 1.25).

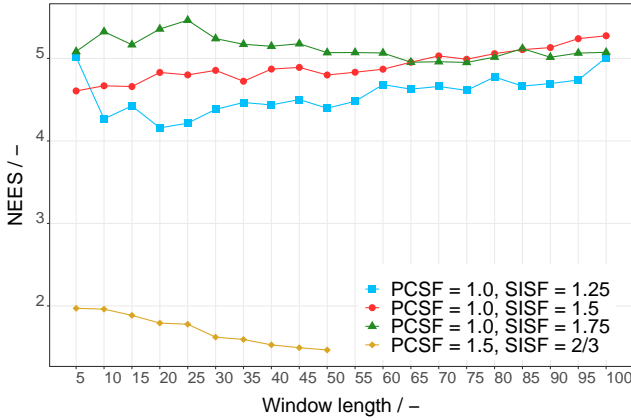


Figure 9. NEES (AVG) of object 2 for different combinations of the SISF and PCSF that define the process noise for the CM (UKF).

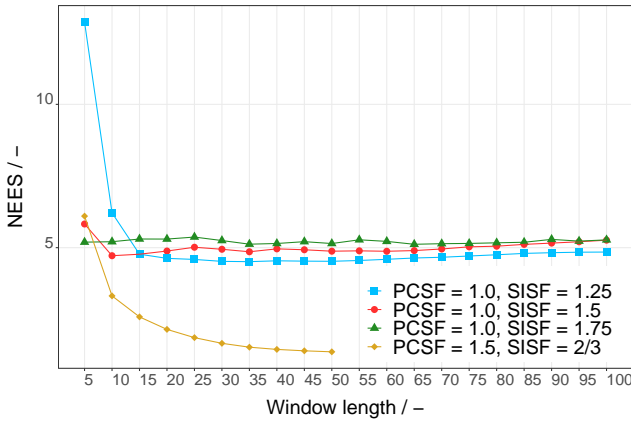


Figure 10. NEES (AVG) of object 2 for different combinations of the SISF and PCSF that define the process noise for the CM (CKF).

Finally, regarding the NIS the results of the UKF and CKF are almost identical. In both cases, very good results with an NIS close 4 can be achieved with either a low window size of 5 and a scaling factor combination of PCSF = 1.0 and SISF = 1.25 or a higher window size of 50 or higher and a scaling factor combination of PCSF = 1.5 and SISF = 2/3. Additionally, a decreasing trend can

be seen clearly for the NIS with increasing window size for all scaling factor combinations.

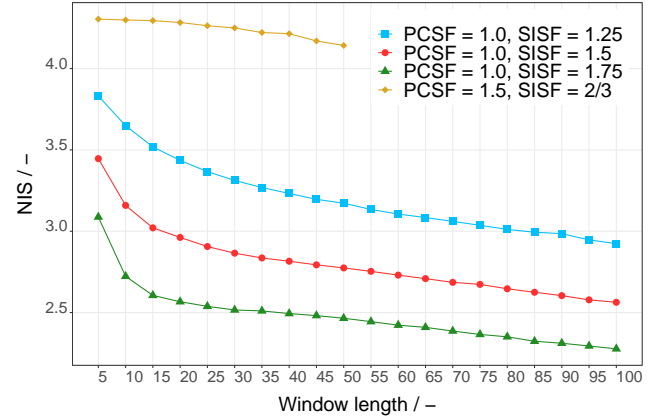


Figure 11. NIS (AVG) of object 2 for different combinations of the SISF and PCSF that define the process noise for the CM (UKF).

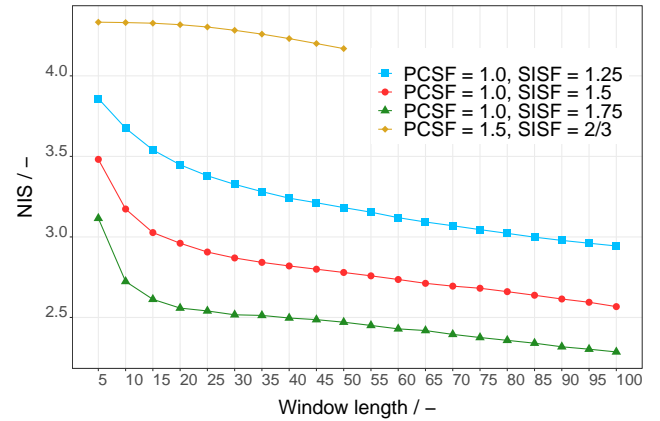


Figure 12. NIS (AVG) of object 2 for different combinations of the SISF and PCSF that define the process noise for the CM (CKF).

To summarize the CM analysis, the RMSE is lowest for the yellow (PCSF = 1.5, SISF = 2/3) and the blue (PCSF = 1.0, SISF = 1.25) data row with a lower window size while the RMSE tends to increase for all combinations of the scaling factors with an increasing window size. Also regarding the NIS the yellow and blue data rows achieve the best results but for different window sizes. The general trend for the NIS is a decrease with an increasing window size. Comparing the UKF and CKF methods the RMSE and NIS are almost identical for both filters. Only regarding the NEES there are significant differences between the UKF and CKF and different combinations of the scaling factors can yield a near-ideal NEES value for different window sizes concerning the CKF. In combination with a relatively low position error, the best choice concerning the UKF and the NEES value is represented by the blue data row (PCSF = 1.0, SISF = 1.25) and an either low window size of 5 or a high window size of

100. Analog to the SNC variations the parameter combinations that achieve the lowest RMSE for the position are not necessarily the best choices regarding realistic results with respect to the covariances. However, regarding the CKF a combination of a low window size, a PCSF of 1.5 and an SISF of 2/3 does indeed combine the lowest RMSE, a very good NEES value and a decent NIS value.

In order to evaluate the results of the ASNC simulations again the RMSE, NEES and NIS are shown. For an additional comparison between the results of two different objects, all results are shown for object 2 and 3. The results shown here represent the second iteration of varying the SISF position components between 0.1 and 0.5 as explained in Section 3. These results are visualized in the same way as was done for the SNC simulations. In this case the shown heatmaps show the results for all 125 combinations of the SISF with the lowest value 0.1 represented by “1” while the others are named accordingly up to 0.5 being represented by “5”. These digit descriptions are, analog to the standard deviations in the SNC variations, used to depict the combinations of the SISF components on the x- and y-axis. The following six plots show the RMSE of the position in the Figures 13 and 14 for object 2 and 3 respectively, the NEES in the Figures 15 and 16 for object 2 and 3 respectively and the NIS in the Figures 17 and 18 for object 2 and 3 respectively.

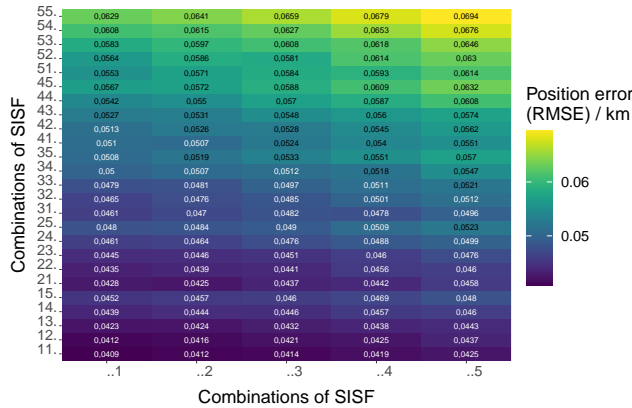


Figure 13. Position error in UVW (RMSE) of object 2 for different combinations of the SISF components that define the process noise for the ASNC (UKF). The x-axis shows the combinations of the third position component, while the y-axis shows the combinations of the two first position components. This heatmap displays all 125 combinations. “1” = 0.1, “2” = 0.2, “3” = 0.3, “4” = 0.4, “5” = 0.5.

While the general magnitude of the RMSE is slightly different for object 2 and 3 the pattern of the results is very similar. In both above plots displaying the RMSE the best results, i.e. the lowest error, is achieved in the lower left area of the heatmap representing the lowest SISF values for the different position components. In the case of object 2 the lowest error is found exactly in the corner at the combination “111” and regarding object 3 the lowest er-

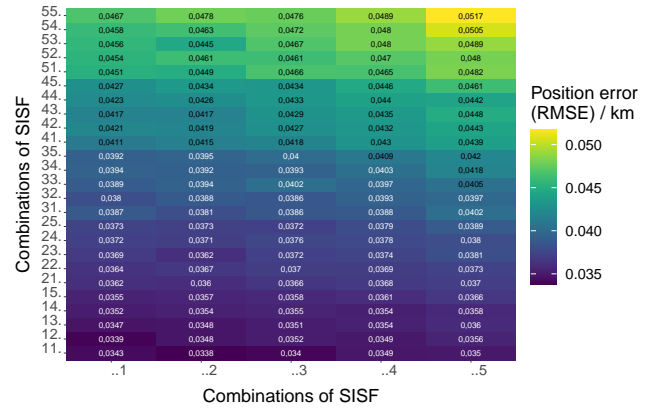


Figure 14. Position error in UVW (RMSE) of object 3 for different combinations of the SISF components that define the process noise for the ASNC (UKF). The x-axis shows the combinations of the third position component, while the y-axis shows the combinations of the two first position components. This heatmap displays all 125 combinations. “1” = 0.1, “2” = 0.2, “3” = 0.3, “4” = 0.4, “5” = 0.5.

ror is achieved by the combination “112”. However, the differences between neighboring fields in the heatmap are small.

Evaluating the heatmaps of the NEES values, the optimal values (close to 6) can be found, fortunately, in the lower left corner as well. Additionally, there is a pattern of better and worse NEES values correlating especially with the second position component. Regarding object 2 the best NEES value is found for the combination “111” matching with the lowest error. For object 3 the best NEES value is found for the combination “121” corresponding to the second lowest error.

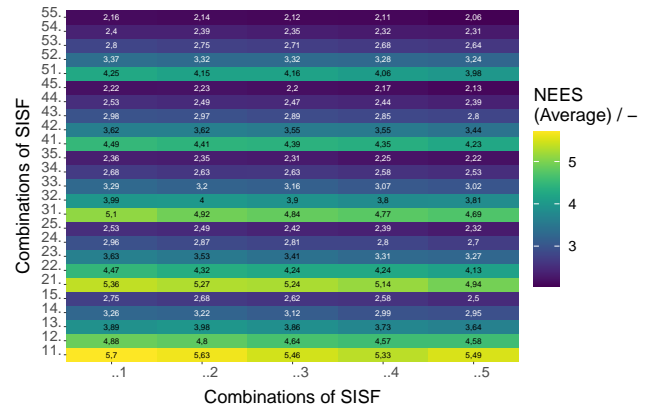


Figure 15. NEES (AVG) of object 2 for different combinations of the SISF components that define the process noise for the ASNC (UKF). The x-axis shows the combinations of the third position component, while the y-axis shows the combinations of the two first position components. This heatmap displays all 125 combinations. “1” = 0.1, “2” = 0.2, “3” = 0.3, “4” = 0.4, “5” = 0.5.

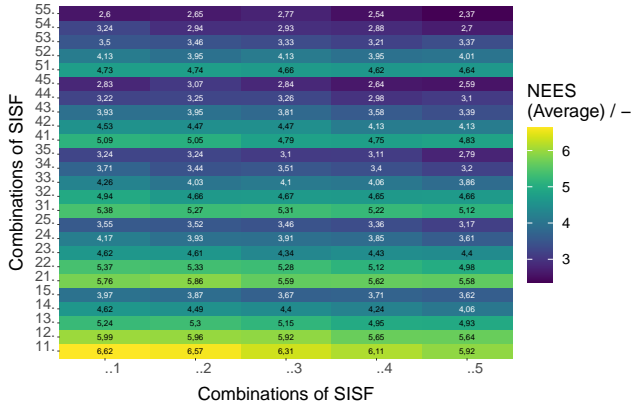


Figure 16. NEES (AVG) of object 3 for different combinations of the SISF components that define the process noise for the ASNC (UKF). The x-axis shows the combinations of the third position component, while the y-axis shows the combinations of the two first position components. This heatmap displays all 125 combinations. “1” = 0.1, “2” = 0.2, “3” = 0.3, “4” = 0.4, “5” = 0.5.

Finally, the NIS shows a similar behavior as seen for the SNC and CM simulation results. Overall the values vary very little, but the general trend is opposed to the trend of the NEES. The best value (closest to 4) tends to be found further to the top right of the heatmap while there is a pattern correlating to the second position component of the SISF analog to the NEES.

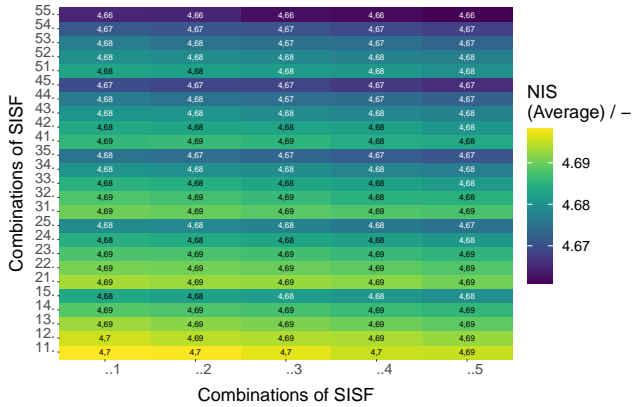


Figure 17. NIS (AVG) of object 2 for different combinations of the SISF components that define the process noise for the ASNC (UKF). The x-axis shows the combinations of the third position component, while the y-axis shows the combinations of the two first position components. This heatmap displays all 125 combinations. “1” = 0.1, “2” = 0.2, “3” = 0.3, “4” = 0.4, “5” = 0.5.

Summarizing the ASNC simulation results, very good overall results can be achieved for a window size of 5, a PCSF of 1.5 and low values for the SISF position components reflecting both a low RMSE for the position and NEES and NIS values close to the optimal of 6 and 4

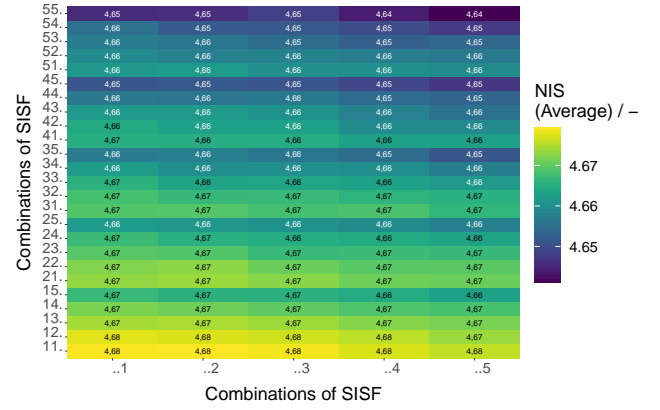


Figure 18. NIS (AVG) of object 3 for different combinations of the SISF components that define the process noise for the ASNC (UKF). The x-axis shows the combinations of the third position component, while the y-axis shows the combinations of the two first position components. This heatmap displays all 125 combinations. “1” = 0.1, “2” = 0.2, “3” = 0.3, “4” = 0.4, “5” = 0.5.

respectively. While the RMSE shows a general trend of decreasing values for decreasing SISFs for all position components, the NEES and NIS seem to be especially sensitive to the second position component. However, all position components have a significant influence and values around 0.1 for the SISF for all three components yield the best overall results.

## 5. CONCLUSION

To summarize the performed analyses and the respective results, Table 3 shows the best results for the different process noise methods extracted from the presented results. If not indicated otherwise, the results in the table represent the simulations for object 2 and the UKF as orbit determination method. The lower half of the table shows the used settings where N is the window length and the last row shows the combination of the position and velocity components of the standard deviation in the case of the SNC and the combination of the position components of the SISF in the case of the ASNC.

In the context of this work, the goal of the performed analyses was an evaluation of the applicability of the adaptive process noise methods, especially the newly developed method ASNC and a comparison with the SNC as a more traditional method. While the results vary slightly between different objects and orbit determination methods, the ASNC proved to have the potential of achieving very good results for the carried out simulations. The usage of the SNC can also lead to very good results if tuned accordingly. This tuning needs a priori knowledge which is the biggest disadvantage of the SNC method. Generally, the CM and ASNC methods only need the window length as a priori known tuning parameter. This was countered by the additional implementation

Table 3. Summary of the best results for the different process noise methods obtained in the simulations presented in this work.

	SNC	CM		ASNC	
	-	UKF	CKF	Obj. 2	Obj. 3
RMSE [km]	0.065	0.122	0.042	0.041	0.034
NEES [-]	5.045	5.016	6.101	5.700	5.990
NIS [-]	4.665	3.832	4.333	4.700	4.680
N [-]	-	5	5	5	5
PCSF [-]	-	1.0	1.5	1.5	1.5
SISF [-]	-	1.25	2/3	var.	var.
Comb. [-]	133111	-	-	111	121

of the scaling factors for the propagated covariance and the state innovation (PCSF and SISF) since this leads to parameters that have to be set correctly before any simulation and therefore need a priori knowledge. In further simulations and analyses it would, therefore, be valuable to evaluate the CM and ASNC methods more comprehensively without these scaling factors. Alternatively, it might be even better to find settings for these factors that are generally applicable and thereby account for errors in the models in an adequate way. Additionally, the analyses should be extended by including a bigger object population and range of different orbits in order to evaluate the different process noise methods in a broader context.

## REFERENCES

1. Stacey, N., D'Amico, S., (2019). Adaptive and Dynamically Constrained Process Noise Estimation for Orbit Determination.
2. NASA, (2020). NASA Spacecraft Conjunction Assessment and Collision Avoidance Best Practices Handbook.
3. Tapley, B. D., Schutz, B. E., Born, G. H., (2004). Statistical Orbit Determination. Elsevier Academic Press. ISBN: 0-12-683630-2
4. Haykin, S., (2001). Kalman Filtering and Neural Networks. John Wiley & Sons, Inc. ISBN 0-471-22154-6.
5. Arasaratnam, I., Haykin, S., (2009). Cubature Kalman Filters. IEEE Transactions on Automatic Control, 54(6), 1254–1269. doi:10.1109/TAC.2009.2019800
6. Myers, K., Tapley, B. (1976). Adaptive sequential estimation with unknown noise statistics. IEEE Transactions on Automatic Control, 21(4), 520–523. doi:10.1109/tac.1976.1101260
7. Meng, Y., Gao, S., Zhong, Y., Hu, G., Subic, A. (2016). Covariance matching based adaptive unscented Kalman filter for direct filtering in INS/GNSS integration. Acta Astronautica, 120, 171–181. doi:10.1016/j.actaastro.2015.12.014
8. Bar-Shalom, Y., Li, X.-Rong, Kirubarajan, T., (2001). Estimation with Applications To Tracking and Navigation. ISBN 0-471-22127-9